

Bio-Inspired Computational Design of Vascularized Electrodes for High-Performance Fast-Charging Batteries Optimized by Deep Learning

Chenxi Sui, Yao-Yu Li, Xiuqiang Li, Genesis Higueros, Keyu Wang, Wanrong Xie, and Po-Chun Hsu*

Slow ionic transport and high voltage drop (IR drop) of homogeneous porous electrodes are the critical causes of severe performance degradation of lithium-ion batteries at high charging rates. Herein, it is numerically demonstrated that a bio-inspired vascularized porous electrode can simultaneously solve these two problems by introducing low tortuous channels and graded porosity, which can be verified by porous electrode theory. To optimize the vasculature structural parameters, artificial neural networks are employed to accelerate the computation of possible structures with high accuracy. Furthermore, an inverse-design searching library is compiled to find the optimal vascular structures under different industrial fabrication and design criteria. The prototype delivers a customizable package containing optimal geometric parameters and their uncertainty and sensitivity analysis. Finally, the full-vascularized cell shows a 66% improvement in charging capacity compared to the traditional homogeneous cell under 3.2 C current density in a numerical simulation. This computational research provides an innovative methodology to solve the fast-charging problem in batteries and broaden the applicability of deep learning algorithms to different scientific or engineering areas.

opportunities for scientists and engineers to overcome conventional hurdles at various aspects and length scales. One bottleneck is the tradeoff between areal capacity and charging rate. Most batteries cannot maintain a high areal capacity under a high charging rate, due to the poor utilization of deep electrode materials.^[3] Although introducing porosity can be helpful, it has to be achieved without sacrificing the cost or energy density at the cell scale. The challenge to overcome the tradeoff between rate performance and mass loading is because randomly-packed porous electrodes tend to be tortuous, which hinders the ion and electron transport within the electrode. Progress has been made to reduce the electrode tortuosity by creating vertical channels through the active material matrix.^[3b,d,e,4] However, complexity arises when considering the non-uniform distribution of the local reaction current density (reaction rate) along

1. Introduction

The development of fast-charging batteries is one of the most essential milestones to push forward the electrification of vehicles and to mitigate the impending crisis of climate and global warming.^[1] As identified by the U.S. Department of Energy, extreme fast charging electric vehicles (EVs) should be able to recharge in less than 10 min to provide 200 miles of driving range.^[2] The ambitious objective poses grand challenges and

with the electrode (active materials) thickness.^[5] Generally, the reaction rate is higher near the separator than that of the current collector, which implies gradual porosity (higher porosity near the separator-electrode interface and lower porosity near the current collector) also plays a vital role in high battery rate performance.^[3a,c,6] Even though both above-mentioned methods (reducing tortuosity and creating graded porosity) could enhance the batteries' fast-charging performance, the best optimization can be realized by introducing both of them. Hence, to achieve fast-charging batteries via porous structure engineering, both porosity distribution and the vertical channel parameters need to be considered, which quickly becomes a highly complex and non-linear design problem.

Nature has already provided plenty of examples to solve this kind of multi-variable transport optimization problem. Billions of years of evolution has created complex transportation system in organisms, such as, plant roots, leaf veins, and blood vessels,^[7] in which vascularized channels are evolved to find the optimal balance between mass transport, metabolic efficiency, and uniformity.^[7a,b,d,8] Inspired by nature, many researchers have designed and manufactured vasculature for efficient transport in applications such as gas sensors, microfluidic systems, and fuel cells.^[9] Therefore, we hypothesize that such a

C. Sui, X. Li, G. Higueros, K. Wang, W. Xie, P.-C. Hsu
Thomas Lord Department of Mechanical Engineering and Materials
Science
Duke University
Durham, NC 27708, USA
E-mail: pochun.hsu@duke.edu
Y.-Y. Li
Department of Chemical Engineering
University of Washington
Seattle, WA 98195, USA

 The ORCID identification number(s) for the author(s) of this article can be found under <https://doi.org/10.1002/aenm.202103044>.

DOI: 10.1002/aenm.202103044

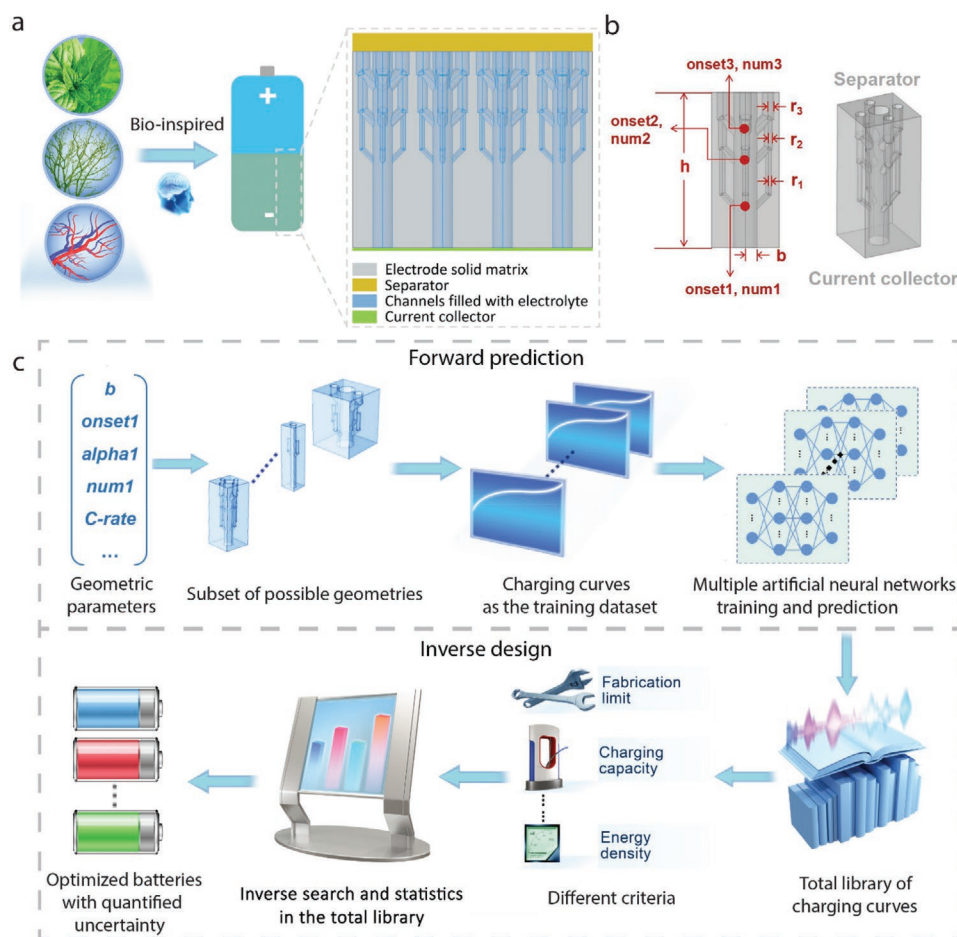


Figure 1. Schematic demonstration of bio-inspired vascular electrode (active materials) and workflow of the deep learning optimization process. a) The bio-inspired vascular channels for fast-charging batteries. b) Vasularized electrode (active materials) geometric model and parameters. The radius of the central channel and the thickness of the electrode (active materials) are expressed as b and h , respectively. Three onset points where the branches grow are defined as $onset1-3$. The number of branches on each onset point are labeled as $num1-3$. The radii of branches, $r1-3$, are obtained by multiplying the central channel radius with a ratio $alpha1-3$. That is, $r = b \times alpha$. We assume the radius of branches on the same onset point are equal. c) The workflow of forward deep learning prediction and inverse design optimization.

vasculature approach can also be applied in Li-ion batteries to accomplish fast-charging without sacrificing material utilization or capacity, as shown in **Figure 1a** and parametrized into the numerical model as **Figure 1b**. Despite having a great potential to outperform traditional methods, the optimization of vascular structures for lithium-ion batteries has not yet been well studied, possibly due to the immense parameter space.

Given the physical governing partial differential equation groups for a Li-ion battery cell and the goal of maximizing charging capacity, there are a few possible approaches to determine the optimal vasculature geometry and parameters. The first is to compute all the charging curves for each geometry by finite element method (FEM). This method works for the highly-simplified scenario as in 1D or even some 2D modeling, but it becomes dramatically time-consuming when considering 3D vasculature design. The second method is topology optimization, a method to find the optimal material spatial distribution for specific objective functions and constraints. Topology optimization has been proven to be a powerful approach for design problems in heat exchangers, structural mechanics,^[10]

and solid oxide fuel cells.^[11] Nonetheless, it is nontrivial for lithium-ion batteries to formalize the objective function and implement topology optimization because the parameters of charging capacity computation are inherently time-dependent, and the Nernst-Planck equation is nonlinear. Prior reports that used topology optimization to study the battery discharging capacity only solved a 2D problem and used the internal resistance as a surrogate for capacity, which could not obtain a distinctive improvement in the end.^[12]

Here, we demonstrate an effective and efficient approach to perform both forward- and inverse-design of vasculature battery electrodes based on deep learning. With the rapid development of data science and artificial intelligence, machine learning algorithms have demonstrated their advantages to solve various optimization problems,^[13] including predicting the optimal operating conditions, charging curves, safety, and synthesis methods concerning Li-ion batteries with promising performances.^[14] To study the influence of vasculature and develop the design tool, we adopt the workflow enabled by the following innovative points: First, we start with the bio-inspired

vascular structures as the initial guesses, which give the artificial neural network (ANN) a time-saving direction to find the optimal geometry. Second, multiple ANNs with bootstrap aggregating (bagging) ensemble algorithm are used for forward- and inverse-design vascular structure to accelerate the computation efficiency 85 times than traditional FEM. Finally, we apply the as-optimized vasculature idea to both cathode and anode, and the vascular full cells show a 66% capacity improvement compared with the homogeneous cell under the U.S. Advanced Battery Consortium's goal for fast-charging electric vehicles' batteries.^[1a]

2. Results and Discussion

2.1. Scheme

The workflow of developing ANNs for vasculature design is illustrated in Figure 1c. The whole process contains the following steps: 1) We created the list of 11 geometric parameters for vasculature (Figure 1b), which is described in Note S1, Supporting Information, in detail. 2) For training dataset generation, we randomly chose 4611 parameter combinations, each of which represents one unique active material's vascular structure. These geometry parameters must also satisfy certain constraints to guarantee the successful formation of the topology structures (e.g., no overlap or penetration). The mass loading and thickness were fixed for all the active materials to ensure a fair comparison. 3) We fed these geometric parameters into finite element modeling software COMSOL Multiphysics to compute the corresponding charging curves, which would serve as the training dataset for our ANNs. As for this massive computation, we discussed the trade-off between the computation cost and accuracy for choosing the mesh in Note S11, Supporting Information. The low variance of the solution by increasing the mesh density (computational degrees of freedom) shows the rationality of our simulation. 4) For the deep learning process, we combined the neural networks and bagging ensemble algorithm to improve the prediction stability and the accuracy of our models. The as-trained neural networks were then used to predict all 389 514 charging curves (64 919 possible vascular structures in our geometric parameter space multiplied by 6 charging rates). 5) We demonstrated inverse design capability by compiling the ANN predicted charging curves as the "inverse searching library," which can be utilized to find the optimal vascular structure under specific targets and limits.

2.2. Electrochemical Analysis for Vascular Structures

Before generating the training dataset and implementing the deep neural networks, we first demonstrate our bio-inspired vasculature idea by choosing specific vascular geometries based on the physical reason for improvement of the vasculature from fundamental electrochemistry and transport theories. We suggest the increased capacity results from the synergistic effect of graded porosity and low tortuosity. The former effect is based on that the total ionic current is larger at the separator side (the boundary condition at the separator/active materials interface

dictates all the current is carried by ions), so lowering the transport resistance near the separator can reduce the overpotential or IR drop, which can be achieved by creating a graded porosity that is more porous near the separator, as depicted in Figure 1a. The porosity is defined by the average porosity at a certain xy -plane and is calculated for all four cells we choose here in Figure S20, Supporting Information. The latter phenomenon is well understood that low tortuosity can increase the effective ion diffusivity in the porous active materials matrix, thereby mitigating the polarization.^[3b,d,e,4a-1] We summarize the comparison between vascularized, vertical channels, and homogeneous electrodes in the spreadsheet in Figure 2a.

To test the above hypothesis, we defined four different electrodes (active materials) unit cells in Figure 2b and computed their charging capacity in COMSOL Multiphysics. Previous researchers have utilized this software to calculate the battery's performance and the results match the experimental data closely.^[15] The geometry models and electrochemical simulation method^[16] are described in Notes S1–S3, Supporting Information. Other geometric factors are: $\alpha3 = 0.5$, $\text{onset3} = 0.14$ mm, $b = 0.005$ mm. Here, the $\alpha3$ is the ratio between the radii of the central channel and branch channels. onset3 is the distance between the 3rd onset point and the current collector. b is the central channel's radius. For a fair comparison, we let all four cells have the same thickness and mass loading, and the minimum channel diameter is also the same for all vascularized channeled electrodes. We computed their charging curves under 5 C charging rate with the cutoff voltage of 4.3 V versus Li/Li⁺. As shown in Figure 2c, the capacity is improved by integrating the vertical channels, consistent with previous research on low tortuous battery electrodes with vertical channels.^[3b,d,e,4a-1] Remarkably, introducing vascular channels further enhances the capacity, which proves our hypothesis that the bio-inspired vasculature can indeed facilitate the electrode design for fast-charging batteries.

For the detailed fundamental electrochemical analysis, we first consider the enhancement by the graded porosity by discussing the penetration depth of Li-ion from the bulk electrolyte (separator side) into the porous electrode (active materials). As studied by Newman et al., the electrodes with higher penetration depth are utilized more efficiently.^[5] The edge of the unit cell is chosen because it is the farthest place from the channels and represents the most extreme scenario (Figure 2b). If more Li ions can diffuse to this location, the electrolyte supply to the whole cell should be better. We plot the Li ion insertion concentration along the edge of unit cells (defined as the red arrow in Figure 2b) under a 10 C charging rate at the cutoff voltage. Note that the top of the unit cell is in contact with the separator (specified in Figure 2b). The concentration decreases dramatically away from the separator due to the depletion of Li ions under high current density (Figure S17, Supporting Information). The zoom-in plot between $x = 0.14$ mm and $x = 0.18$ mm (Figure 2d) shows that vascular branches increase the local Li-ion concentration. As seen in Figure 2d, the more branches we have near the separator, the higher Li-ion insertion concentration, and reaction penetration depth. Higher Li-ion insertion concentration indicates more Li-ion diffuse into the active materials, and the electrochemical reaction penetrates deeper, explaining the function of the vasculature.

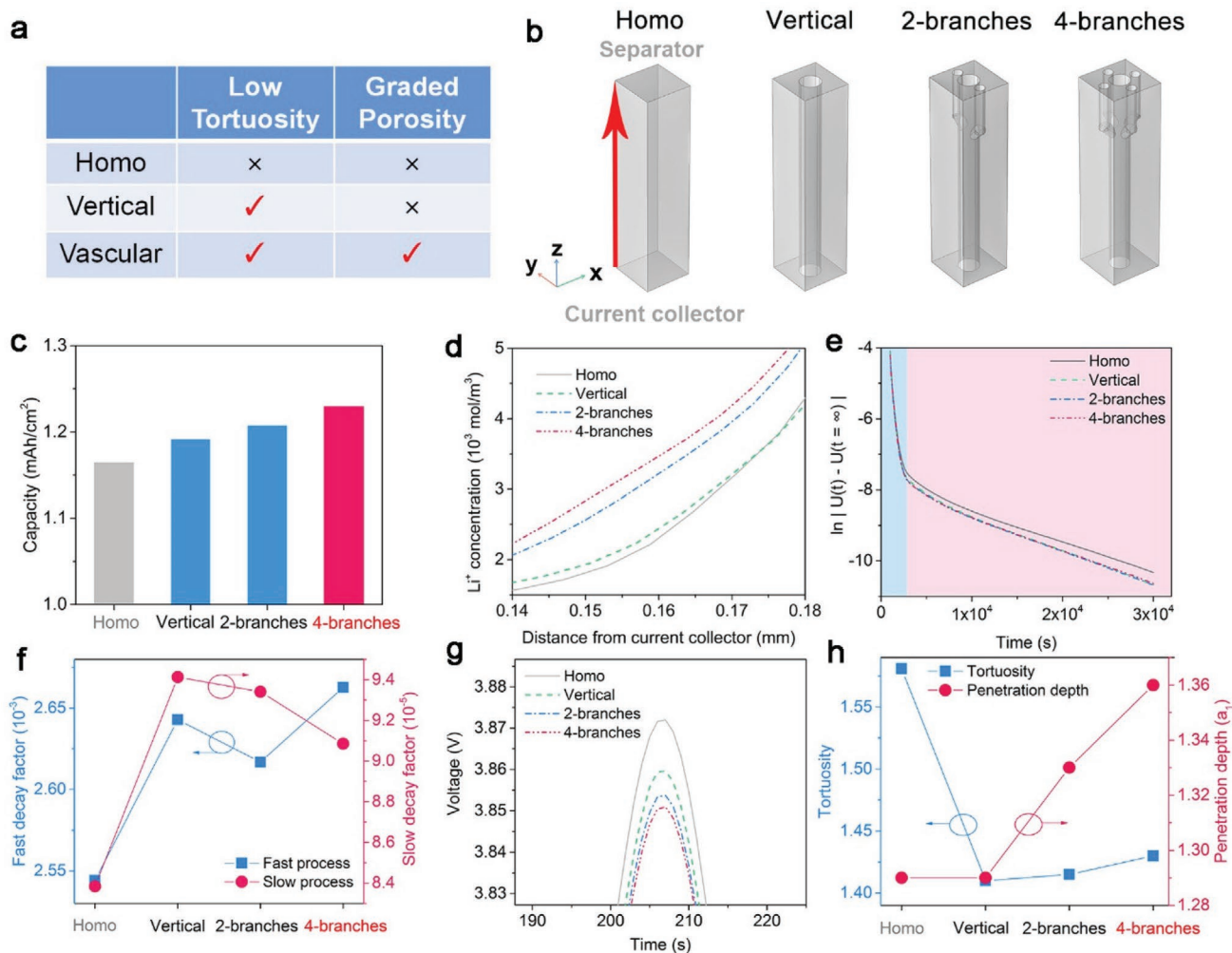


Figure 2. Electrochemical comparative analysis of different electrode structures. a) The table compares homogenous (traditional) electrodes, vertical channel electrodes, and our vascular channel electrodes. Two critical factors are identified: Tortuosity and graded porosity. b) The unit cells in this calculation. The vascular channels are located near the active materials-separator interface. The red cutline is the edge of the unit cell, which is used for the Li-ion insertion concentration calculation. c) The charge capacity of various electrode structures under 5 C. d) The zoomed-in figure of the Li ion insertion concentration profile in the x-axis range from 0.14 to 0.18 mm under 10 C. The cutline is defined in (b). e) DC depolarization test. Two linear diffusion processes are present: The fast kinetic process in blue shadow: 1000–2000 s and the slow kinetic process in red shadow: 2000–30 000 s. f) The fitted slopes of different electrode geometries for fast (1000–2000 s) and slow (2000–30 000 s) diffusion processes, which represent the voltage decay factors. g) Zoomed-in high C-rate pulse charging figure for one pulse process. h) Calculated tortuosity and penetration depth with the physical model near the active materials-separator interface concerning different geometries.

The second factor is the reduced tortuosity, which is characterized by the DC depolarization test. Figure S18, Supporting Information, shows the voltage profile of the polarization-depolarization process. The cell is first charged under 0.1 C current for 1000 s and then relaxed for 49 000 s to reach the equilibrium potential $U(t = \infty)$ ($\Delta U/\Delta t < 0.1 \text{ mV h}^{-1}$). As reported by Li et al.,^[3e] the kinetic process is described as the slope of the logarithm linear fit of $U(t) - U(t = \infty)$, which represent the potential decay factor below:

$$\ln |U(t) - U(t = \infty)| = \text{const} - \frac{t}{t^\delta} \quad (1)$$

where $1/t^\delta$ is the decay factor. The higher the absolute value of the slope is, the faster the voltage would decay to equilibrium

potential, demonstrating an improved kinetic process of the electrode. The curves in Figure 2e show two different kinetic processes. In the beginning (from 1000 to 2000 s in the blue shaded region), the high slopes represent the fast kinetic process, mainly contributed by the ionic electronic diffusion in the electrolyte liquid phase. Then, after the fast kinetic process, a slow kinetic process follows (red shaded region), which corresponds to the diffusion of Li ions from solid active materials particles to liquid electrolyte. In Figure 2f, we plot the slopes (or voltage decay factors) of different geometric active materials under these two processes. Vertical channels increase the decay factors from 2.544×10^{-3} to 2.643×10^{-3} for a fast process and from 8.38×10^{-5} to 9.41×10^{-5} for a slow process, respectively. The decay factors remain similar values by branching out more vascular channels (2-branch and 4-branch). This makes physical

sense because the channels are straight, and their radii are on the same order of magnitude, which suggests similar tortuosity.

The two physical factors listed above provide the vasculature with high C-rate capacity improvement, which can be characterized by the high C-rate pulse charging. The lower voltage during the high C-rate pulse charge indicates the IR drop is reduced by the vasculature. The whole pulsed charge process is demonstrated in Figure S19, Supporting Information. One representative pulse process is shown in Figure 2g for detailed analysis. At the end of the charging process, the lowest voltage of 4-branches vasculature represents the enhanced high-rate charging performance due to the reduced tortuosity and graded average porosity at a certain xy-plane. Such improvement is also consistent with a previous study.^[6a]

To provide more physical insights, we use tortuosity and penetration depth to quantify the electrochemical transport capability of different electrode configurations and to analyze the limiting factors of the porous electrodes. The tortuosity of electrodes is calculated as described in Note S4, Supporting Information. On the other hand, the penetration depth quantifies how thick the electrode (active materials) could be effectively used by chemical reaction (Li-ion insertion). This value is derived by solving the partial differential equation groups given by Newman et al.^[5] The final expression is written below:

$$\frac{L}{\nu} = a_1 \sqrt{\frac{1}{1-\varepsilon}} \quad (2)$$

where L is the thickness of the electrode, ν is the parameter of nonuniformity defined as

$$\nu = L \sqrt{c \frac{\kappa + \sigma}{\kappa \sigma}} \quad (3)$$

c is the slope of polarization equation, κ and σ are the conductivity of electrolyte and active materials,^[17] a_1 is a constant (see details in Note S5, Supporting Information) and ε is the average porosity of active materials at the certain xy-plane to characterize the local transport properties near the separator/active materials interface. According to Newman's theory, the larger ν is, the distribution of the Li^+ insertion reaction is more nonuniform (much higher near the separator).^[17] The derivation of this penetration depth is shown in Note S5, Supporting Information. (Here, the geometric factors are the same as the above calculation: $\alpha_3 = 0.5$, $\text{onset}_3 = 0.14$ mm, $b = 0.005$ mm). The definition of geometric parameters is the same as above (Figure 1b). Specifically, higher tortuosity and/or larger penetration depth lead to high charging capacity. We plot the tortuosity and penetration depth near the separator-active materials interface for different geometry in Figure 2h. Apparently, the tortuosity decreases by introducing channels into the porous active materials, consistent with previous research results.^[3b,d,e,4a-1] The penetration depth increases gradually with more branching channels near the separator-active materials interface by providing a higher average porosity at the xy-plane in this region (Equation (2)). The higher average porosity near the separator of the vascularized electrode with more branches could be validated by calculating the average porosity in Figure S20, Supporting Information. Results from the theoretical models agree

well with the electrochemical analysis in Figure 2c–g, which not only proves our bio-inspired idea of vasculature but serves as a practical design guideline for future development.

2.3. Artificial Neural Network Development and Performance

The success of these specific vasculatures invites a comprehensive optimization among all geometry parameters. More importantly, we desire to obtain the capability to inverse-design the ideal vasculature based on particular practical requirements or limitations. Considering the enormously complex parameter space to describe the vasculature, we think machine learning is a great method to speed up the process. After comparing the advantages and disadvantages of prevailing machine learning (ML) algorithm^[18] (Discussion, Supporting Information), we decided to utilize deep learning as a part of the optimization and design tools. The details of our ANNs structure and the bagging ensemble algorithm are described in Note S6, Supporting Information. In Figure 3a, the fully overlapped charging curves (the blue solid lines represent FEM simulation, and the red dash lines represent ANN prediction) and the corresponding low mean square error (MSE) under different charging rates and geometries show excellent prediction accuracy of our neural networks. The low validation MSE loss of $\approx 10^{-4}$ indicates that we successfully avoid the overfitting issue (Figure 3b). In Figure 3c, the simulated and predicted capacity values aligned closely with the $y = x$ line with a high R^2 value of 0.9995, also suggesting high prediction accuracy. The key advantage of our ANNs is achieving high-fidelity prediction of charging curves with a much smaller demand for computational power compared to the exhaustive combinatorial FEM. As shown in Figure 3d, our deep learning model is 84 times faster than the total FEM in screening the parameters and building the total library. Detailed time calculation is shown in Note S6, Supporting Information.

2.4. Electrodes Inverse Design under Different Criteria

Compared with the forward prediction of the charging curve for each geometry and rate, battery manufacturers are often more interested in understanding what vascular channel structure has the best performance under various kinds of constraints. For example, the optimized geometries would be different when the fabrication resolution is different (influence the smallest channel radius), or when the power density should not exceed a given value for safety concerns. However, such inverse design problems are generally more challenging because of the complicated geometric parameters of vasculature and the nonlinearity of objective functions,^[19] especially in time-dependent models such as, batteries. Therefore, we take advantage of the forward-prediction computation efficiency and accuracy of our ANNs and construct a total library storing the information such as charging curves, active materials channel structures, charging rates, theoretical capacity, and average porosity at a certain xy-plane. From this total library, we can rank the performance under certain practical requirements/limits of manufacturability, cost, or C-rate. To make the library

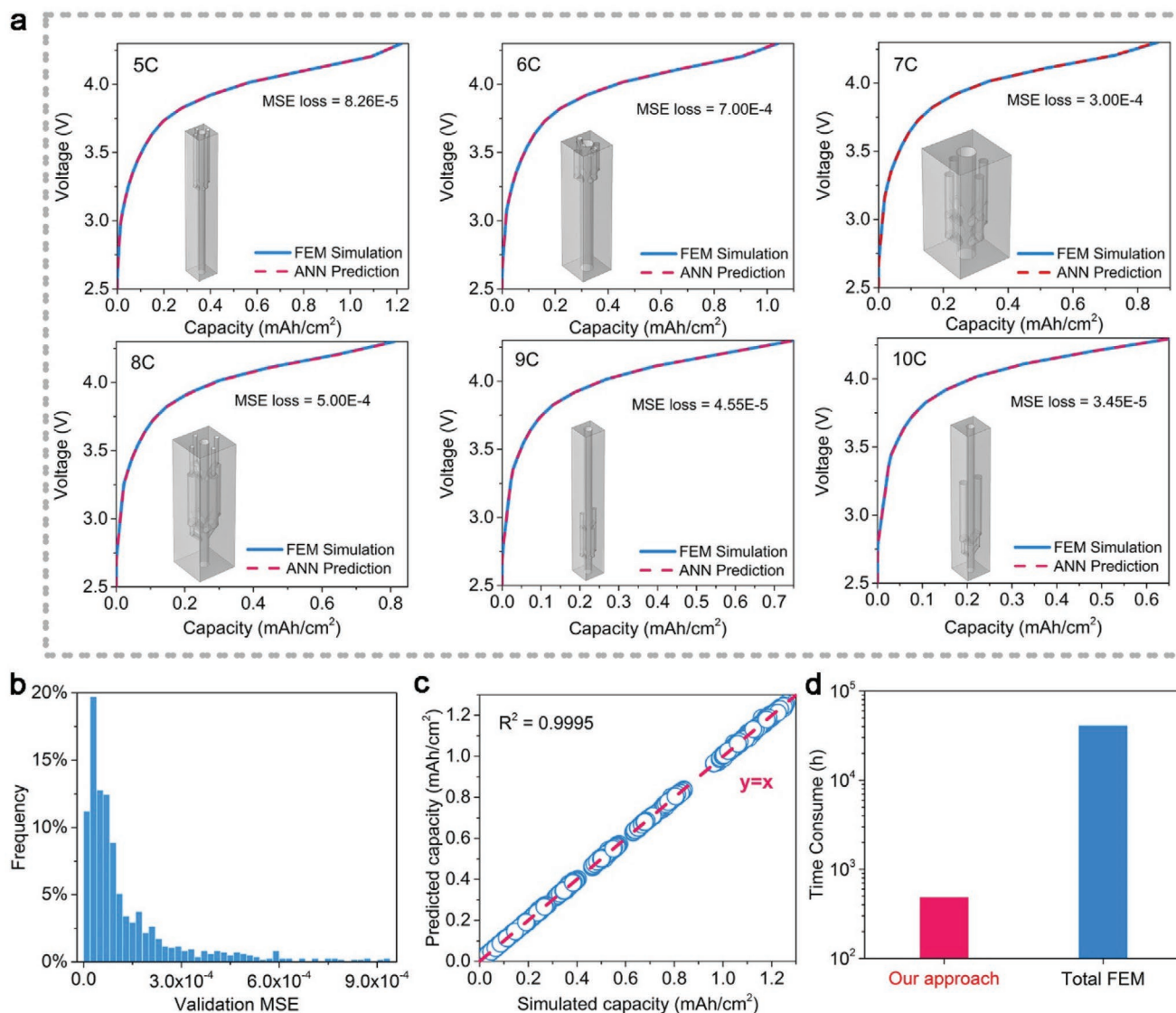


Figure 3. Artificial neural network training performance. a) Comparison of predicted and simulated charging curves under different C-rates and vasculatures. The geometric parameters for these 6 geometries are listed in the Table S6, Supporting Information. Each curve consists of 20 data points evenly spaced along the y-axis (Figure S11, Supporting Information). The mean square error (MSE) loss of the simulation is presented in the upper right corner. b) The histogram of the validation test MSE. Most of the validation MSEs are smaller than 3.0×10^{-4} . c) Correlation between simulated data and ANN predicted data. All data points are aligned near $y = x$ representing the high accuracy of the trained neural network. d) Computation time for building the total library using our deep learning prediction versus traditional finite element computation.

more comprehensive, we also add other useful electrochemical properties such as energy density, average voltage, and power density of each vascular structure. This approach is inspired by the “fast forward dictionary search,” which was first demonstrated by Nadell et al. to be a powerful design tool for all-dielectric metasurfaces.^[20] For batteries, the major differences besides the physical laws are the time-dependent behaviors and the emphasis on high charging capacity rather than specific peak features.

For the inverse design problems, after combining a given optimization target with an additional industrial fabrication limit (e.g., the smallest channel radius possible to fabricate, the low power density limitation for efficient charging, etc.), we can

easily find the optimal vascular structures by searching in the total library constructed by forward prediction. Such inverse design workflow for finding the optimized geometries adapting certain requirements is demonstrated in Figure 4a. Herein, we give two optimization scenarios: A (find the maximum capacity under 5 C and the minimum channel radius is 0.01 mm) and B (find the maximum energy density under 10 C with the low power density limitation and the minimum channel radius is 0.005 mm) for demonstration. Details for calculating power density, energy density, and more specific inverse design method description are written in Note S6, Supporting Information. The optimal top two geometries among the top three branch number configurations are listed in Table S4,

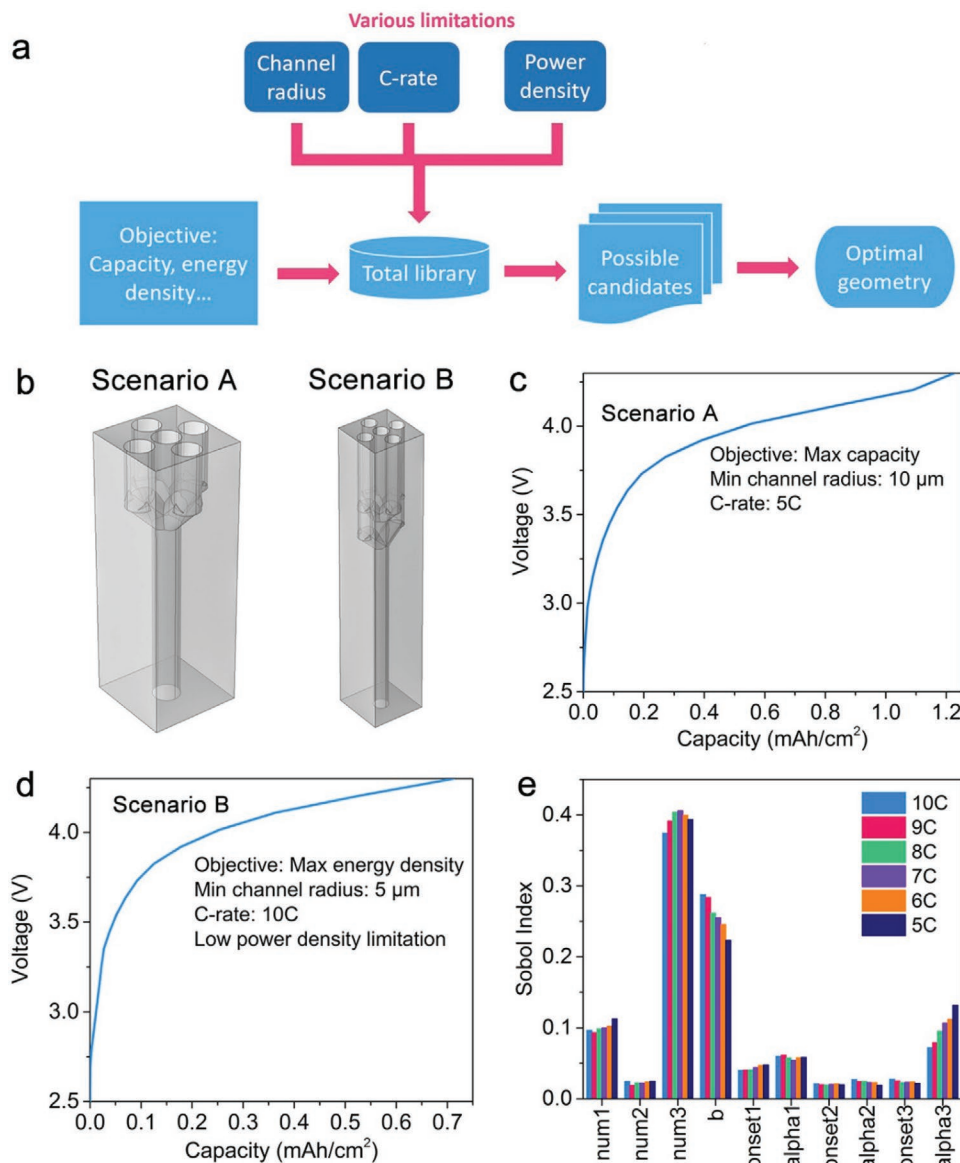


Figure 4. Customized inverse design package. a) Workflow of inverse design. b) The optimized geometries for scenarios A and B. c,d) Predicted charging curves for scenarios A and B. e) Global sensitivity analysis for each geometry parameter shown by Sobol Index.

Supporting Information. We select the top one geometry for each scenario and draw them in Figure 4b. It is obvious the optimized geometries for high charging capacity and energy density still follow the “more branches near the separator” rule. The porosity profiles analysis for different branches number configurations also supports the general rule (Notes S7 and S8, Supporting Information), making our inverse design method more convincing. Apart from the geometric parameters, our inverse design method can also provide the optimal geometries’ corresponding charging curves (Figure 4c,d) The different optimal results of branches number configurations between scenarios A and B demonstrate the importance and necessity of our inverse design method, because the cells with high charging capacity or energy density may also come at the price of the high overpotential (represented by the high charging

power for the same C-rate) that is not desired for charging efficiency. Thus, the inverse design can effectively provide the cell’s geometry for different industrial applications that have various technical limitations, such as, fabrication size limitation, charging power density limitation, and waste heat generation. With the comprehensive library compiled by the efficient ANN, the inverse problems are no longer challenging even with the highly complicated geometric parameters of the vasculature.

2.5. Global Sensitivity Analysis (Sobol’s Method)

In practice, there can be fabrication errors in microchannel geometry and solid matrix porosity that influence the prediction accuracy. In other words, although the vasculatures

designed by ANNs and the total library work well for COMSOL Multiphysics modeling, the realistic deviation might influence the accuracy for real-world batteries. Therefore, we use Sobol's method to analyze the sensitivity of each parameter on charging capacity to determine the robustness and significance of these parameters (Note S9, Supporting Information).^[21] Another benefit of sensitivity analysis is to help correlate the theory and simulation in real numbers. In Figure 4e, we can see that the Sobol index for $num3$ is the largest, which indicates the number of branches on the onset node 3 has the highest impact on charging capacity. This result agrees well with the theory because the ionic current near the separator-active materials interface region is much higher than that near the current collector. Apart from the number of branches in this region, branch radius (expressed by the ratio to central channel radius α_{1-3}) will also impact the average porosity at certain xy-plane, although not as significantly as the branch number. If the branch radius is larger near the active materials-separator interface, the average porosity at xy-plane would be increased, and the capacity would be enhanced. Central channel radius b is another significant factor because it changes the unit cell size when the areal mass loading and electrode thickness are fixed. If the unit cell is larger, the lateral transport distance of Li-ion from the channel to the corner of the unit cell would be longer, slowing down the ion transport.^[3b]

2.6. Full-Cell Results

Based on the enhancement by the vascular channels in graphite anode, it is promising to apply the configurations on both anode and cathode and further boost the fast-charging performance at the full-cell level (Figure 5a). The model computation method is described in Notes S2 and S3, Supporting Information. Need to note that the dimensions of the channel radius is 5 μm . Such resolution is possible to achieve with the help of the two-photon polymerization method.^[22] Figure 5b shows the charging capacities for different structured electrodes under 5 and 10 C charging rates. The vascular branching channels give the battery a higher improvement than vertical channels, no matter it is anode-structured or double-structured. The best performance is delivered by the double vascular battery, which is as high as 1.18 and 0.476 mAh cm^{-2} areal capacity under 5 and 10 C charging rates, respectively. That means 43.9% and 13.94% improvement compared to homogeneous electrodes are realized (for 5 and 10 C charging rates). Even compared with the half vertical channels case, the double vascularized battery still possesses 39.72% and 8.06% improvement under 5 and 10 C charging rates. Since the overall porosity of all the batteries here is the same, the results again prove the ion transport improvement and IR drop reduction induced by vascular structures. The considerable improvement shines the light on a fast-charging battery in real industrial production by the bio-inspired vasculature idea.

The U.S. Advanced Battery Consortium's goal for fast-charging electric vehicles' batteries is to charge to 80% capacity within 15 min.^[1a] If we assume a constant charging process, the charging rate should be at least 3.2 C. In Figure 5c, such a current is used to charge the homogeneous porous

electrodes (40% overall porosity) battery and double vascular full-cell batteries (both cathode and anode are vascularized with 40% overall porosity). The double vascular full-cell battery uses the same vascular geometry as listed in Table S3, Supporting Information. The capacity of the double vascular full cell is 2.119 mAh cm^{-2} , almost 66% larger than that of the homogeneous electrode. All electrochemical parameters are the same as in Table S2, Supporting Information.

We further test the vascularized full cells with pulse charging (Figure 5d). The pulse charging current configuration is set as the smooth periodic piece-wise function to ensure convergence of computation. The cell is charged under a 15 C charging rate for 0.2 s and then rest for 0.2 s under zero current. The process is repeated until the voltage reaches the cutoff voltage (4.3 V). Because of the low tortuosity and graded porosity, the double vascular full-cell battery exhibits a larger capacity (pulse charging for 22.98 s) than a regular homogeneous counterpart (pulse charging for 16.98 s). Such 1.35-time improvement clearly demonstrates the effectiveness of vasculature design for high-rate charging performance.

2.7. Potential Experimental Realization

Although computationally optimized vascular structures are more complicated than the traditional random particles made by the slurry-coating method, there are several feasible approaches for fabrication, thanks to the rapid development of additive manufacturing and microfabrication technology. Herein, we propose three promising fabrication methods that can be utilized to prepare the vascularized structures with the necessary resolution, reproducibility, and scalability for wide-range applicability: i) Photolithography; ii) high-resolution 3D-printing (e.g., two-photon polymerization); and iii) vertically channeled stratified slurry coating. The following paragraphs discuss the methods mentioned above in detail.

The first method is photolithography. The authors combined the "sacrificial template" method^[3b] and photolithography microfabrication to accomplish the vascular electrodes. The experimental steps for sacrificial templates and vascular channels coin cells fabrications are shown in Figures S27 and S28, Supporting Information. The detailed steps are described in Discussion, Supporting Information. With the help of this fabrication method, we can fabricate electrodes with at least 2-branches vascular channels. According to the computation results, 2-branches can also improve the battery rate performance (Figure 2c). Figure S29, Supporting Information, shows the scanning electron microscope images of the as-fabricated vascularized electrodes, proving the as-designed vasculature can be successfully fabricated. Photolithography is the core technology in modern integrated circuit manufacturing, and the explosive increase of the semi-conductor sales^[23] shows the reproducibility and scalability of such a photolithography microfabrication method.

The second method is high-resolution 3D printing. The most suitable technique among them is two-photon polymerization, which has been regarded to have high resolution but low speed. Encouragingly, recent work in 2019 showed 10 000 times improvement in print speed at a fraction of cost.^[24] Two-photon

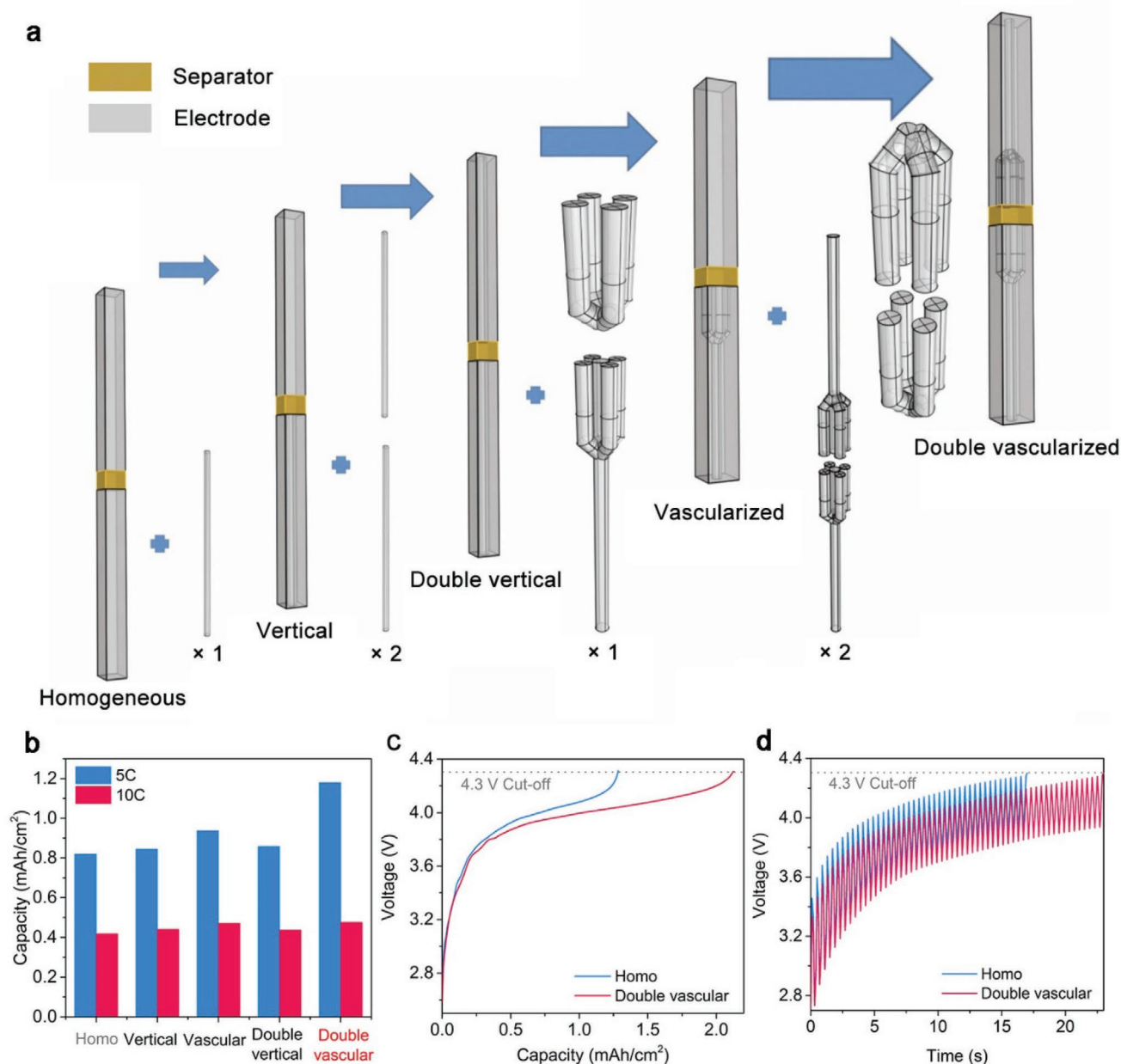


Figure 5. The full-cells simulation for real application scenarios. a) The schematic for designing full cells with traditional vertical channels and vascular channels. Each of the cases represents the unit cell for that kind of geometry. The charging performance enhances gradually by introducing more vasculatures. b) Charging capacity comparison between different configurations under 5 and 10 C charging rates. The vascularized structure shows a significant improvement, and the double vascular structure possesses the best performance. c) Charging curves comparison under the U.S. Advanced Battery Consortium’s goal (3.2 C). d) High-rate pulse charged curves comparison.

polymerization can fabricate the 4-branches sacrificial templates described previously, and the subsequent preparation steps are the same. This method can easily achieve the desired resolution of the as-designed vasculature. Even the current printing speed is not sufficiently high, it is hopeful of elevating its production speed to a large-scale level in the near future.

Last but not least, to further simplify the experimental procedure for low-cost and large-scale fabrication, we propose the “vertically channeled stratified slurry coating” method based on

the fundamental transport and diffusion theory elaborated in this paper. From studying the bio-inspired vascular structure design, we realized that the fundamental physical principle to enhance the ionic transport inside the porous electrode is to create gradual porosity and low-tortuosity channels. Vasculature is one structure to satisfy both criteria, but it is not the only structure. In principle, the vascular structure can be replaced by a vertically channeled electrode with graded porosity. The stratified slurry with gradual porosity can be achieved by the

differential sedimentation method,^[3a] and the vertical channels can be created using the method in previous reports by Chiang et al.^[3b] Slurry coating and sacrificial template methods are both well-developed and thus are of reproducibility and scalability. Since the fundamental physical principles of the vasculature (gradual porosity and low-tortuous channels) are encoded into the structure, this method can be quickly scaled up to realize the fast-charging performance improvement achieved by the vasculature.

It is worthwhile to mention that all these experimental methods to fabricate porous electrodes structure are supported and guided by the fundamental electrochemical and transport principles and numerical modeling developed in this work. Our computational work is essential to understand the governing physics to provide the inverse design methodology and avoid trial-and-error experiments for better work efficiency.

3. Conclusions

In this article, the bio-inspired vasculature approach to address the performance degradation of Li-ion batteries under a high charging rate is presented. The fundamental electrochemical theory explains that the vascularized porous electrode improves the fast-charging performance in two ways. First, it reduces the tortuosity of the active materials. Second, the hierarchical branches of vascular structures create gradual porosity distribution profiles. Among them, the graded profiles with high average porosity near the separator-active materials interface will improve the performance by suppressing the IR-drop of the whole system. We demonstrated an efficient deep-learning prototype to predict and inverse-design the vascular structures under different criteria. Finally, full-cell analysis was conducted and showed vasculature can realize a 66% improvement under 3.2 C constant current charge and a 35% improvement of charging time under 15 C pulse-charge, compared to the homogeneous batteries. Looking beyond batteries, this work could also potentially serve as an innovative methodology for optimizing the topological design of complex 3D transportation systems which cannot be solved analytically, such as, flow-based gas catalysis,^[25] biological diffusion systems,^[26] and other reactive flow problems. We also correlated our predicted results with potential experimental realizations and identified the limitations (simplified limited parameter space and potential choices of other deep learning tools) of this work (also see Discussion, Supporting Information). We want to point out that this computational design work has to be the prerequisite for the experimental realization of vascularized electrodes, due to the massive parameters space. We hope this could inspire future fast-charging batteries experimental and theoretical advancement.

4. Experimental Section

Finite Element Computation: The battery charging simulation was conducted using the COMSOL Multiphysics Li-ion battery Module. All electrochemical simulation parameters and geometric model were described in Notes S1–S3, Supporting Information. The massive parametric sweeping was achieved by the Cluster Sweep feature and the software is run on 400 CPUs supported by Duke Compute Cluster.

Deep Learning: The ANNs were constructed using PyTorch (1.9.0 + CUDA 10.2 version) open-source machine learning library. All details about the structure, input parameters, and output results are described in Supporting Information 6. The neural network training was conducted on the GPU supported by Duke Compute Cluster.

Supporting Information

Supporting Information is available from the Wiley Online Library or from the author.

Acknowledgements

C.S. and Y.-Y.L. contributed equally to this work. The authors would like to thank Prof. Willie Padilla and Dr. Omar Khatib for the valuable discussion regarding artificial neural network development and inverse design strategy. The authors would also like to thank Prof. Jon Herman (UC Davis, Department of Civil and Environmental Engineering) for kindly helping with the sensitivity analysis and COMSOL Multiphysics Inc. for the technical support on simulation. Hao Zhang (Duke University, Civil and Environmental Engineering Department) also provided a useful discussion on the data analysis. This work was supported by North Carolina Space Grant. The authors also thank the Pratt School of Engineering at Duke University for the funding support.

Conflict of Interest

The authors declare no conflict of interest.

Author Contributions

P.-C.H. and C.S. conceived the idea. C.S. performed the finite element simulation and electrochemical theoretical analysis. C.S. and Y.-Y.L. performed the neural network training and prediction. C.S. and Y.-Y.L. performed inverse design optimization. C.S. performed the global sensitivity analysis. G.H. helped with the design of vascular structures. K.W. helped with porosity distribution analysis. X.L. helped with data processing and presenting. W.X. helped with figures. C.S., Y.-Y.L., and P.-C.H. wrote the manuscript with input from all co-authors.

Data Availability Statement

The data that support the findings of this study are available from the corresponding author upon reasonable request.

Keywords

bio-inspired vasculature, deep learning, fast-charging batteries

Received: September 30, 2021

Revised: December 8, 2021

Published online: December 30, 2021

[1] a) Y. Liu, Y. Zhu, Y. Cui, *Nat. Energy* **2019**, *4*, 540; b) M. Rogge, S. Wollny, D. Sauer, *Energies* **2015**, *8*, 4587.

[2] C. J. Michelbacher, S. Ahmed, I. Bloom, A. Burnham, B. Carlson, F. Dias, E. J. Dufek, A. N. Jansen, M. Keyser, D. Howell, S. Boyd, B. Cunningham, S. Gillard, L. Siezak, K. Hardy, P. A. Nelson, D. C. Robertson, T. Stephens, R. Vijayagopal, M. Mohanpurkar,

- D. Scofield, M. Shirk, T. Tanim, C. Kruezer, O. Li, A. Markel, A. Meintz, A. Pesaran, S. Santhanagopalan, K. Smith, E. Wood, J. Zhang, *Enabling Fast Charging: A Technology Gap Assessment*, <https://doi.org/10.2172/1466683> (Accessed: December 2021).
- [3] a) Y.-M. Chiang, B. Hellweg, Reticulated and Controlled Porosity Battery Structures, *US Patents, US 7553584 B2* **2001**; b) C.-J. Bae, C. K. Erdonmez, J. W. Halloran, Y.-M. Chiang, *Adv. Mater.* **2013**, *25*, 1254; c) Z. Du, D. L. Wood, C. Daniel, S. Kalnaus, J. Li, *J. Appl. Electrochem.* **2017**, *47*, 405; d) Y. Kuang, C. Chen, D. Kirsch, L. Hu, *Adv. Energy Mater.* **2019**, *9*, 1901457; e) L. Li, R. M. Erb, J. Wang, J. Wang, Y.-M. Chiang, *Adv. Energy Mater.* **2019**, *9*, 1802472.
- [4] a) J. Billaud, F. Bouville, T. Magrini, C. Villevieille, A. R. Studart, *Nat. Energy* **2016**, *1*, 16097; b) J. S. Sander, R. M. Erb, L. Li, A. Gurijala, Y. M. Chiang, *Nat. Energy* **2016**, *1*, 16099; c) F. Shen, W. Luo, J. Dai, Y. Yao, M. Zhu, E. Hitz, Y. Tang, Y. Chen, V. L. Sprenkle, X. Li, L. Hu, *Adv. Energy Mater.* **2016**, *6*, 1600377; d) C. Chen, Y. Zhang, Y. Li, Y. Kuang, J. Song, W. Luo, Y. Wang, Y. Yao, G. Pastel, J. Xie, L. Hu, *Adv. Energy Mater.* **2017**, *7*, 1700595; e) Y. Li, K. K. Fu, C. Chen, W. Luo, T. Gao, S. Xu, J. Dai, G. Pastel, Y. Wang, B. Liu, J. Song, Y. Chen, C. Yang, L. Hu, *ACS Nano* **2017**, *11*, 4801; f) J. Luo, X. Yao, L. Yang, Y. Han, L. Chen, X. Geng, V. Vattipalli, Q. Dong, W. Fan, D. Wang, H. Zhu, *Nano Res.* **2017**, *10*, 4318; g) Y. Zhang, W. Luo, C. Wang, Y. Li, C. Chen, J. Song, J. Dai, E. M. Hitz, S. Xu, C. Yang, Y. Wang, L. Hu, *Proc. Natl. Acad. Sci. U. S. A.* **2017**, *114*, 3584; h) R. Amin, B. Delattre, A. P. Tomsia, Y.-M. Chiang, *ACS Appl. Energy Mater.* **2018**, *1*, 4976; i) B. Delattre, R. Amin, J. Sander, J. De Coninck, A. P. Tomsia, Y.-M. Chiang, *J. Electrochem. Soc.* **2018**, *165*, A388; j) C. Huang, P. S. Grant, *J. Mater. Chem. A* **2018**, *6*, 14689; k) L. L. Lu, Y. Y. Lu, Z. J. Xiao, T. W. Zhang, F. Zhou, T. Ma, Y. Ni, H. B. Yao, S. H. Yu, Y. Cui, *Adv. Mater.* **2018**, *30*, 1706745; l) Z. Zhao, M. Sun, W. Chen, Y. Liu, L. Zhang, N. Dongfang, Y. Ruan, J. Zhang, P. Wang, L. Dong, Y. Xia, H. Lu, *Adv. Funct. Mater.* **2019**, *29*, 1809196; m) F. L. E. Usseglio-Viretta, W. Mai, A. M. Colclasure, M. Doeff, E. Yi, K. Smith, *Electrochim. Acta* **2020**, *342*, 136034.
- [5] J. Newman, K. E. Thomas-Alyea, *Electrochemical Systems*, John Wiley & Sons, Hoboken, NJ **2012**.
- [6] a) V. Ramadesigan, R. N. Methekar, F. Latinwo, R. D. Braatz, V. R. Subramanian, *J. Electrochem. Soc.* **2010**, *157*, A1328; b) K. Song, W. Li, Z. Chen, X. Wu, Q. Zhou, K. Snyder, L. Zhang, *Ionics* **2021**, *27*, 1261.
- [7] a) C. D. Murray, *Proc. Natl. Acad. Sci. U. S. A.* **1926**, *12*, 207; b) T. F. Sherman, *J. Gen. Physiol.* **1981**, *78*, 431; c) M. C. White, D. B. Marin, D. V. Brazeal, W. H. Friedman, *Hum. Relat.* **1997**, *50*, 1383; d) G. B. West, J. H. Brown, B. J. Enquist, *Science* **1999**, *284*, 1677.
- [8] S. K. Hetz, T. J. Bradley, *Nature* **2005**, *433*, 516.
- [9] a) M. Kayla, *Masters Thesis*, University of Maine **2019**; b) J.-H. Huang, J. Kim, N. Agrawal, A. P. Sudarsan, J. E. Maxim, A. Jayaraman, V. M. Ugaz, *Adv. Mater.* **2009**, *21*, 3567; c) B. D. Hatton, I. Wheelton, M. J. Hancock, M. Kolle, J. Aizenberg, D. E. Ingber, *Sol. Energy Mater. Sol. Cells* **2013**, *117*, 429; d) N. Guo, M. C. Leu, U. O. Koylu, *Int. J. Hydrogen Energy* **2014**, *39*, 21185; e) C. Howell, T. L. Vu, J. J. Lin, S. Kolle, N. Juthani, E. Watson, J. C. Weaver, J. Alvarenga, J. Aizenberg, *ACS Appl. Mater. Interfaces* **2014**, *6*, 13299; f) X. Zheng, G. Shen, C. Wang, Y. Li, D. Dunphy, T. Hasan, C. J. Brinker, B.-L. Su, *Nat. Commun.* **2017**, *8*, 14921; g) K. Marquis, B. Chasse, D. P. Regan, A. L. Boutiette, A. Khalil, C. Howell, *Adv. Biosyst.* **2020**, *4*, 1900216.
- [10] a) R. Xue, R. Li, Z. Du, W. Zhang, Y. Zhu, Z. Sun, X. Guo, *Extreme Mech. Lett.* **2017**, *15*, 139; b) X. Zhu, C. Zhao, X. Wang, Y. Zhou, P. Hu, Z.-D. Ma, *Eng. Optim.* **2019**, *51*, 1687.
- [11] a) C. Kim, H. Sun, *Int. J. Automot. Technol.* **2012**, *13*, 783; b) X. Song, A. R. Diaz, A. Benard, Presented at *Proceedings of the 10th World Congress on Structural and Multidisciplinary Optimization*, Orlando, Florida **2013**.
- [12] X. Tianchi, *Master of Engineering*, Delft University of Technology, **2015**.
- [13] L. Bottou, F. E. Curtis, J. Nocedal, *SIAM Rev.* **2018**, *60*, 223.
- [14] a) W. Li, J. Zhu, Y. Xia, M. B. Gorji, T. Wierzbicki, *Joule* **2019**, *3*, 2703; b) P. M. Attia, A. Grover, N. Jin, K. A. Severson, T. M. Markov, Y.-H. Liao, M. H. Chen, B. Cheong, N. Perkins, Z. Yang, P. K. Herring, M. Aykol, S. J. Harris, R. D. Braatz, S. Ermon, W. C. Chueh, *Nature* **2020**, *578*, 397; c) A. Bhowmik, T. Vegge, *Joule* **2020**, *4*, 717; d) Y. Zhang, Q. Tang, Y. Zhang, J. Wang, U. Stimming, A. A. Lee, *Nat. Commun.* **2020**, *586*, E11; e) D. P. Finegan, J. Zhu, X. Feng, M. Keyser, M. Ulmefors, W. Li, M. Z. Bazant, S. J. Cooper, *Joule* **2021**, *5*, 316; f) J. Tian, R. Xiong, W. Shen, J. Lu, X.-G. Yang, *Joule* **2021**, *5*, 1521.
- [15] a) J. Park, J. Jeong, Y. Lee, M. Oh, M.-H. Ryou, Y. M. Lee, *Adv. Mater. Interfaces* **2016**, *3*, 1600140; b) R. Zahn, M. F. Lagadec, M. Hess, V. Wood, *ACS Appl. Mater. Interfaces* **2016**, *8*, 32637; c) X. Xu, Y. Liu, J. Y. Hwang, O. O. Kapitanova, Z. Song, Y. K. Sun, A. Matic, S. Xiong, *Adv. Energy Mater.* **2020**, *10*, 2002390.
- [16] a) K. Smith, C.-Y. Wang, *J. Power Sources* **2006**, *160*, 662; b) R. Zhao, J. Liu, F. Ma, *J. Electrochem. Energy Convers. Storage* **2020**, *17*, 021111.
- [17] N. John, T. Charles, *J. Electrochem. Soc.* **1962**, *109*, 1183.
- [18] a) Y. Reich, S. V. Barai, *Artif. Intell. Eng.* **1999**, *13*, 257; b) R. Caruana, A. Niculescu-Mizil, Presented at *Proceedings of the 23rd International Conference on Machine Learning*, **2006**, pp. 161–168; c) I. Nitze, U. Schulthess, H. Asche, *Proceedings of the 4th GEOBIA, Rio de Janeiro, Brazil* **2012**, *79*, 3540; d) J.-C. Huang, K.-M. Ko, M.-H. Shu, B.-M. Hsu, *Neural Comput. Appl.* **2019**, *32*, 5461.
- [19] G. Chavent, *Nonlinear Least Squares for Inverse Problems: Theoretical Foundations and Step-by-Step Guide for Applications*, Springer Science & Business Media, Berlin **2010**.
- [20] C. C. Nadell, B. Huang, J. M. Malof, W. J. Padilla, *Opt. Express* **2019**, *27*, 27523.
- [21] a) I. M. Sobol, *Math. Comput. Simul.* **2001**, *55*, 271; b) J. Herman, W. Usher, *J. Open Source Software* **2017**, *2*, 97; c) N. C. Do, S. Razavi, *Water Resour. Res.* **2020**, *56*, e2019WR025436.
- [22] a) K.-S. Lee, D.-Y. Yang, S. H. Park, R. H. Kim, *Polym. Adv. Technol.* **2006**, *17*, 72; b) X. Zhou, Y. Hou, J. Lin, *AIP Adv.* **2015**, *5*, 030701.
- [23] T. Sueyoshi, Y. Ryu, *Energies* **2020**, *13*, 5998.
- [24] S. K. Saha, D. Wang, V. H. Nguyen, Y. Chang, J. S. Oakdale, S.-C. Chen, *Science* **2019**, *366*, 105.
- [25] D. G. Wheeler, B. A. W. Mowbray, A. Reyes, F. Habibzadeh, J. He, C. P. Berlinguette, *Energy Environ. Sci.* **2020**, *13*, 5126.
- [26] C. Tomasina, T. Bodet, C. Mota, L. Moroni, S. Camarero-Espinosa, *Materials* **2019**, *12*, 2701.